Contents lists available at ScienceDirect

# Solar Energy Materials and Solar Cells

journal homepage: http://www.elsevier.com/locate/solmat

# NiCr–MgF$_2$ spectrally selective solar absorber with ultra-high solar absorptance and low thermal emittance

Yuping Ning [a,b], Jian Wang [a,*], Chunhui Ou [a], Changzheng Sun [a], Zhibiao Hao [a], Bing Xiong [a], Lai Wang [a], Yanjun Han [a], Hongtao Li [a], Yi Luo [a,**]

[a] *Department of Electronics Engineering, Tsinghua University, Beijing, 100084, China*
[b] *Institute of Microelectronics, Tsinghua University, Beijing, 100084, China*

## ARTICLE INFO

## ABSTRACT

NiCr–MgF$_2$ spectrally selective solar absorber, which consists of the tandem films of Au, high-metal-volume-fraction (HMVF) NiCr–MgF$_2$, low-metal-volume-fraction (LMVF) NiCr–MgF$_2$ and MgF$_2$, is designed and fabricated for ultra-high solar absorptance and low thermal emittance. The performance of Au/NiCr–MgF$_2$ (HMVF)/NiCr–MgF$_2$ (LMVF)/MgF$_2$ is simulated using the effective medium theory and film matrix method, and the optimized NiCr–MgF$_2$ spectrally selective solar absorber has a normal solar absorptance ($\alpha_{sn}$) of 0.981 and a normal thermal emittance ($\varepsilon_n$) of 0.042 at 25 °C. The tandem films of Au/NiCr–MgF$_2$ (HMVF)/NiCr–MgF$_2$(LMVF)/MgF$_2$ are fabricated by magnetron sputtering and measured by UV-VIS-IR spectrometer, and it has an ultra-high near normal solar absorptance of $\alpha_{sn} = 0.976$ and a low near normal thermal emittance of $\varepsilon_n = 0.045$ at 25 °C, which approaches very closely to the simulated limit. Furthermore, NiCr–MgF$_2$ spectrally selective solar absorber allows a wide incident angle ($\theta$) with its angular solar absorptance $\alpha_s(\theta) \geq 0.957$ and angular thermal emittance $\varepsilon(\theta) \leq 0.054$ if $\theta \leq 50°$. Such spectrally selective solar absorber is an outstanding candidate for solar thermal applications.

## 1. Introduction

Spectrally selective solar absorber captures and converts sunlight into thermal energy [1], and they are applied to solar hot water systems [2], concentrated solar power (CSP) plants [3–9], solar thermoelectric generators [10] and solar thermophotovoltaics [11]. To maximize photo-thermal conversion efficiency, the solar absorber should have high solar absorptance ($\alpha_s$) in the solar spectrum range (0.3–2.5 μm) and low thermal emittance ($\varepsilon$) in the infrared (IR) range ($\lambda > 2.5$ μm) [12–18].

Thus far, various solar absorbers have been widely investigated, for example, (1)intrinsic absorbers [19], (2)semiconductor-metal tandems [20], (3)multilayer stacks [21], (4)metal-dielectric (cermet) composite absorbers [12], (5)textured surfaces [22], and (6)selectively solar-transmitting coatings on blackbody-like absorbers [21]. Among them, cermet based solar absorbers have been attracting the attention of researchers due to their excellent performance on the spectral selectivity, i.e. high $\alpha_s$ and low $\varepsilon$ [23–25]. When metal nanoparticles are

imbedded in the dielectric matrix, the cermet layer strongly absorbs solar radiation due to interband transitions in metal together with small particle resonances and becomes relatively transparent in IR range. This enables a high spectral selectivity for the cermet based solar absorber [1, 12,26,27]. Using Cr$_2$O$_3$, Al$_2$O$_3$, AlN, SiO$_2$ and ZrO$_2$ based cermet as absorption layer, the solar absorbers have demonstrated outstanding optical properties [28–34]. For the experimentally optimized cermet based solar absorbers, the values of solar absorptance and thermal emittance are mostly 0.93–0.96 and 0.05–0.10 for temperatures from 25 to 100 °C, respectively [28,30,33]. To date, the Ni–NiO cermet based solar absorber [24] is known to show the best spectral selectivity ($\alpha_s/\varepsilon$) being 0.969/0.047. How to improve the spectral selectivity of the cermet based solar absorber further is still an urgent and severe challenge.

The purpose of our research work is to achieve solar absorber with superior spectral selectivity. For this target, an optimal coating structure, appropriate materials and optimization method for the developed solar absorber are prepared. Firstly, a double cermet layer structure,

providing an optimal spectral selectivity for the solar absorber, is adopted [35]. Secondly and crucially, optically optimal dielectric materials for the cermet absorption layer and antireflection layer are chosen. The dielectric materials with lower refractive index ($n$), can make the sunlight sufficiently permeate into the solar absorber, which is benefit for enhancing solar absorption. In addition, the antireflection layer with lower refractive index material brings a better antireflective effect for sunlight, improving solar absorption further [23]. Compared with the above dielectric material for cermet layers ($n$(AlN) = 2.13, $n$ ($Cr_2O_3$) = 2.12, $n$($ZrO_2$) = 2.12, $n$($Al_2O_3$) = 1.67, $n$($SiO_2$) = 1.47 at $\lambda = 1\,\mu m$), the $MgF_2$ ($n$($MgF_2$) = 1.37 at $\lambda = 1\,\mu m$) has the lowest refractive index [36–41]. Hence, $MgF_2$ is selected as the dielectric material for the cermet and the antireflection layers in order to maximize solar absorption. The alloy NiCr is chosen as the light absorbing metal component in the cermet layers. Compared with low cost metals, e.g. Al and Cu, Au film has higher reflectance in IR range and is adopted as the IR reflector in our absorber. Finally, a theoretically optimization process, based on the effective medium theory and film matrix method [23, 24,42,43], is carried out to acquire the optimal parameters for the NiCr–$MgF_2$ cermet based solar absorber before preparation.

In this paper, a novel Au/NiCr–$MgF_2$ (HMVF)/NiCr–$MgF_2$ (LMVF)/ $MgF_2$ solar absorber with the double cermet layer structure, is theoretically optimized and fabricated by magnetron sputtering. The fabricated solar absorber is found to have an extremely high near normal solar absorptance of 0.976 and a low near normal thermal emittance of 0.045 at 25 °C. To the best of our knowledge, this is the best spectral selectivity reported so far. Furthermore, the NiCr–$MgF_2$ cermet based solar absorber allows a wide incident angle ($\theta$) with its angular solar absorptance $\alpha_s(\theta) \geq 0.957$ and angular thermal emittance $\varepsilon(\theta) \leq 0.054$ if $\theta \leq 50°$.

## 2. Theoretical model

The spectral selectivity of a solar absorber is evaluated by the solar absorptance and thermal emittance. The angular solar absorptance $\alpha_s(\theta)$, angular thermal emittance $\varepsilon(\theta)$ and hemispherical thermal emittance $\varepsilon_h$ are defined by Eqs. (1)–(3), respectively,

$$\alpha_s(\theta) = \frac{\int_{0.3\mu m}^{2.5\mu m} (1 - R(\theta, \lambda)) I_s(\lambda) d\lambda}{\int_{0.3\mu m}^{2.5\mu m} I_s(\lambda) d\lambda} \tag{1}$$

$$\varepsilon(\theta) = \frac{\int_{2.5\mu m}^{100\mu m} (1 - R(\theta, \lambda)) I_b(\lambda, T) d\lambda}{\int_{2.5\mu m}^{100\mu m} I_b(\lambda, T) d\lambda} \tag{2}$$

$$\varepsilon_h = \frac{\int_0^{\pi/2} \int_{2.5\mu m}^{100\mu m} \sin(2\theta)(1 - R(\theta, \lambda)) I_b(\lambda, T) d\lambda d\theta}{\int_{2.5\mu m}^{100\mu m} I_b(\lambda, T) d\lambda} \tag{3}$$

where $I_s(\lambda)$, $I_b(\lambda, T)$ and $R(\theta, \lambda)$ are respectively the solar radiation spectrum, blackbody radiation spectrum at 25 °C and angular reflectance spectrum of the solar absorber [25,44]. The normal solar absorptance and normal thermal emittance are marked as $\alpha_{sn}$ and $\varepsilon_n$, respectively. The photo-thermal conversion efficiency $\eta$ is introduced to characterize the compromise of normal solar absorptance and hemispherical thermal emittance as [25]:

$$\eta = \alpha_s - \frac{\varepsilon_h \sigma T^4}{CI} \tag{4}$$

where $\sigma$, $T$, $C$, and $I$ are Stefan-Boltzmann constant, working temperature of solar absorber, concentration ratio and solar radiation,

respectively. In our simulation, the conditions are as follows: $T = 25$ °C, $C = 2.3$ and $I = 1000$ Wm$^{-2}$.

The double cermet layer structure of the NiCr–$MgF_2$ cermet based solar absorber consists of four layers (Fig. 1) [35]: (1) An antireflection (AR) $MgF_2$ layer that enhances the transmission of solar radiation by antireflection. (2) HMVF and LMVF cermet layers which absorb solar radiation by the combination of intrinsic and interference absorption. (3) An IR-reflector Au layer, which has high reflectance in IR region to reduces the thermal emittance. The thickness of the Au layer is ~100 nm, which is optically opaque in IR region. The HMVF and LMVF cermet layers are composed of many NiCr and $MgF_2$ minilayers which are alternately deposited. The expected metal volume fraction is adjusted by the current and deposition times of the NiCr and $MgF_2$ minilayers.

The optical constants (refractive index $n$ and extinction coefficient $k$) of Au, Ni, Cr and $MgF_2$ are obtained from Refs. [41,45,46]. The optical constants of alloy NiCr in the cermet layer are calculated by Eq. (5):

$$\tilde{n}\left(\text{NiCr}\right) = \sqrt{\frac{4\tilde{n}(\text{Ni})^2 + \tilde{n}(\text{Cr})^2}{5}} \tag{5}$$

where $\tilde{n} = n + ik$ is the complex refractive index [47]. The Bruggeman model based on the effective medium theory [23], is adopted to calculate the optical constants of the NiCr–$MgF_2$ cermet layer. Having acquired the optical constants of the four layers, the reflectance spectra of this NiCr–$MgF_2$ cermet based multilayer solar absorber are calculated using the film matrix approach [48]. Finally the values of solar absorptance, thermal emittance and photo-thermal conversion efficiency are calculated according to Eqs. (1)–(4).

## 3. Experimental section

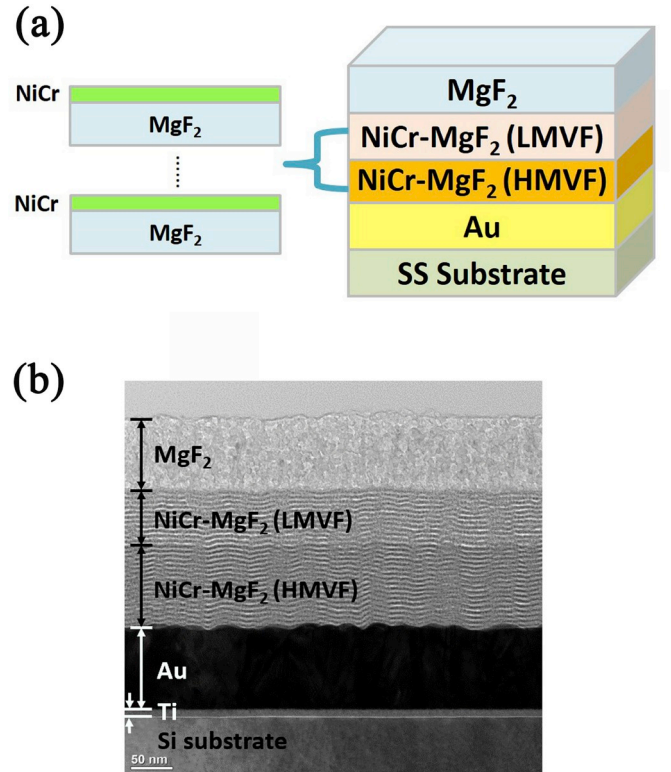The stainless steel (SS)/Au/NiCr–$MgF_2$ (HMVF)/NiCr–$MgF_2$



**(a)**

**(b)**

**Fig. 1.** (a) Schematic diagram and (b) cross-sectional TEM micrograph of the Au/NiCr–$MgF_2$ (HMVF)/NiCr–$MgF_2$ (LMVF)/$MgF_2$ solar absorber.

(LMVF)/MgF$_2$ solar absorber is prepared using magnetron sputtering systems. The size of all the targets is $200 \times 60 \times 3$ mm$^3$. An Au (99.99% purity) target, a Ni–Cr alloy (Ni$_4$Cr, 99.95% purity) target and an MgF$_2$ (99.99% purity) target are used to deposit the Au metal layer, NiCr–MgF$_2$ cermet layers and MgF$_2$ layer. The NiCr–MgF$_2$ cermet layers are prepared by sputtering metal NiCr and dielectric MgF$_2$ alternately. The polished SS substrates are cleaned with acetone followed by ethanol using an ultrasonic cleaner. The base pressure of the chamber of magnetron sputtering system is pumped to $4 \times 10^{-4}$ Pa. Table 1 shows the detailed fabrication parameters for the NiCr–MgF$_2$ cermet based solar absorber.

The reflectance spectra in 0.3–2.5 μm and 2.5–24 μm are measured using Cary 5000 UV–Vis–NIR and Bruker Vertex 80 FT-IR spectrometers, respectively. The near normal reflectance spectra in 0.3–2.5 μm and 2.5–24 μm are measured using an integrating sphere accessory with incident angle of $3°40'$ and an A519 VW mirror reflectance accessory with incident angle of 12°, respectively. The angular reflectance spectra in 0.3–2.5 μm and 2.5–24 μm are measured by a UMA angular reflectance accessory (6–80°) and an A513/Q angular reflectance accessory (15–80°), respectively. The reflectance values in 25–100 μm are extrapolated referring to standard EN 673 [27]. The cross-sectional image of the solar absorber deposited on Si substrate are measured using FEI Tecnai TF-20 transmission electron microscopy (TEM). The thickness of the absorber is determined from the cross-sectional micrograph [49]. The reflectance and transmittance spectra in 0.3–2.5 μm of the NiCr–MgF$_2$ cermet layers deposited on quartz substrate are measured by Cary 5000 UV–Vis–NIR spectrometer. The optical constants of the NiCr–MgF$_2$ cermet layers are fitted by the matrix formulation approach [48,50] based on the reflectance, transmittance and thickness.

## 4. Results and discussion

### 4.1. Theoretical optimization of solar absorber

#### 4.1.1. Effect of metal volume fractions

The refractive index ($n(\lambda)$) and absorption coefficient ($\alpha(\lambda) = 4\pi k(\lambda)/\lambda$) of the NiCr–MgF$_2$ cermet layers with different metal volume fractions ($f$) on the wavelength are calculated by effective medium theory (Fig. 2 (a) and (b)). The measured $n(\lambda)$ and $\alpha(\lambda)$ of the deposited NiCr–MgF$_2$ cermet layers with $f = 0.13$ and 0.25 agree well with the calculated values (Fig. 2 (c) and (d)). The $n(\lambda)$ of MgF$_2$ and $\alpha(\lambda)$ of NiCr are also plotted in Fig. 2 (a) and (b), respectively, for the designed tandem films. According to Kirchhoff's law, an ideal cermet layer of solar absorber needs to have high $\alpha(\lambda)$ in solar spectrum range ($\lambda \in [0.3, 2.5]$ μm) and zero $\alpha(\lambda)$ in thermal emission range ($\lambda \geq 2.5$ μm). It is observed that in reality NiCr–MgF$_2$ cermet does not exhibit ideal spectral selectivity features. As shown in Fig. 2 (b), NiCr–MgF$_2$ cermet with $f \leq 0.4$ has a certain degree of spectral selectivity, i.e., greater $\alpha(\lambda)$ in $\lambda \in [0.3, 2.5]$ μm than that in $\lambda \geq 2.5$ μm, and under consideration of cermet to selectively absorb solar radiation. However, the solar absorption coefficient and spectral selectivity of cermet are contradictory. The cermet with higher metal volume fraction has greater $\alpha(\lambda)$, which is helpful to absorb solar radiation under the condition of effective antireflection. The cermet with higher metal volume fraction is found to

exhibit less difference in the absorption coefficient between solar spectrum range and thermal emission range of the solar absorber. Therefore, metal volume fractions in both LMVF and HMVF NiCr–MgF$_2$ need to be chosen carefully to compromise solar absorption and spectrally selectivity. Moreover, individual layers with different metal volume fractions have different $n(\lambda)$ and $k(\lambda)$, which lead to reflection at interfaces. Such reflection is not good for absorbing solar radiation, but is helpful to suppress the thermal radiation by reflecting the incident infrared radiation. Therefore, the combination of thicknesses of individual layers also need to be optimized to minimize the reflection in solar spectrum range and maximize the reflection in IR range. These contribute to effective absorption of solar radiation and suppression of IR radiation.

Metal volume fractions of LMVF ($f_L$) and HMVF ($f_H$) NiCr–MgF$_2$ are chosen in the range of 0.1–0.2 and 0.2–0.4, respectively. NiCr–MgF$_2$ with metal volume fraction of $f_L$ has good spectral selectivity and the counterpart with $f_H$ absorbs solar radiation effectively. Combination of $f_L$ and $f_M$ is also for the effective reflection in IR radiation due to the big differences of $n$ and $k$ of individual layers in IR region.

#### 4.1.2. Effect of layer thicknesses

Thicknesses of MgF$_2$ ($d_{AR}$)、LMVF NiCr–MgF$_2$ ($d_{LMVF}$) and HMVF NiCr–MgF$_2$ ($d_{HMVF}$) are optimized with the optically opaque Au (100 nm) on the substrate for constructive interference absorption to solar radiation and keeping high reflectance in IR region by transfer matrix. Fig. 3 shows the simulated normal solar absorptance and normal thermal emittance of NiCr–MgF$_2$ solar absorber as a function of thicknesses of MgF$_2$, LMVF and HMVF NiCr–MgF$_2$, where $d_{AR}$, $d_{LMVF}$ and $d_{HMVF}$ are in the range of 0–200 nm and metal volume fractions of LMVF and HMVF NiCr–MgF$_2$ are 0.17 and 0.32, respectively. As shown in Fig. 3 (a), the normal solar absorptance is mainly determined by LMVF and HMVF NiCr–MgF$_2$, whose critical thicknesses are about 50–100 nm for effective absorption of solar radiation. Fig. 3 (b) shows the set of dots of [$d_{AR}$, $d_{LMVF}$, $d_{HMVF}$] whose corresponding normal solar absorptance are not less than 0.970, and the maximum normal solar absorptance is 0.983 at [$d_{AR}$, $d_{LMVF}$, $d_{HMVF}$] = [86, 82, 174] nm. These dots form a relatively big volume in the space of [$d_{AR}$, $d_{LMVF}$, $d_{HMVF}$]. It indicates a wide process window of high-solar-absorptance for NiCr–MgF$_2$ solar absorber arising out of low $n$ and $k$ of MgF$_2$ in UV-VIS-IR range. As shown in Fig. 3(c), the normal thermal emittance of NiCr–MgF$_2$ absorber is mainly determined by HMVF NiCr–MgF$_2$, and the thicker HMVF NiCr–MgF$_2$ results in higher normal thermal emittance. It can be observed that in the IR range ($\lambda \geq 2.5$ μm), the MgF$_2$ and LMVF NiCr–MgF$_2$ have extremely low absorption coefficients, resulting negligible effect of the thickness $d_{AR}$ and $d_{LMVF}$ on the normal thermal emittance. Fig. 3 (d) shows the set of dots of [$d_{AR}$, $d_{LMVF}$, $d_{HMVF}$] whose corresponding $\varepsilon_n \leq 0.050$. Fig. 3 (e) shows the set of dots of [$d_{AR}$, $d_{LMVF}$, $d_{HMVF}$] whose corresponding $\alpha_{sn} \geq 0.970$ and $\varepsilon_n \leq 0.050$. As marked in Fig. 3(e) and listed in Table 2, the maximal $\eta$ is 0.971 at [$d_{AR}$, $d_{LMVF}$, $d_{HMVF}$] = [84, 77, 137] nm and [$f_{LMVF}$, $f_{HMVF}$] = [0.17, 0.32], and the corresponding normal solar absorptance and normal thermal emittance are 0.981 and 0.042, respectively.

#### 4.1.3. Effect of incident angles

Spectral reflectance at near normal incidence is usually measured to characterize optical property of solar absorber. Actually, the solar absorptance is strongly dependent on the incident angle of sunlight on the absorber surface due to the varied position of the sun with time. Therefore it is valuable for solar absorber to have high absorptance at wide incident angle range for both CSP and non-CSP applications [32, 43,51–54]. Fig. 4 shows the simulated absorptance spectra of the optimized solar absorber at different incident angles from 0° to 90°. The optimized solar absorber shows an excellent spectral selectivity over a wide angular range from 0° up to 50°. As the condition of constructive interference absorption is not valid at big incident angles, the absorptance in solar spectrum range decreases significantly and thus the solar absorptance deteriorates if incident angle is greater than 50°. While the
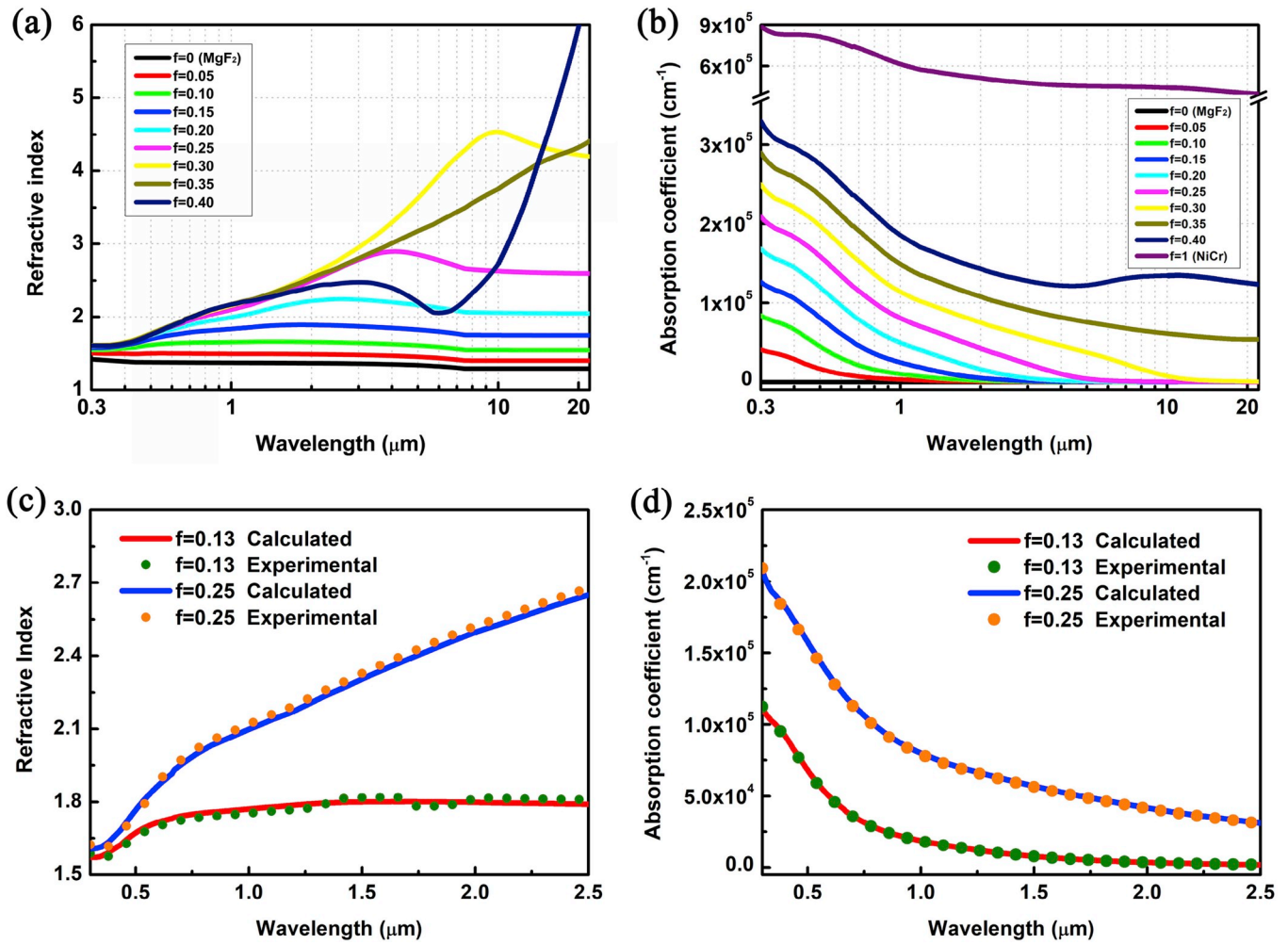
**Table 1**
The deposition parameters of the Au/NiCr–MgF$_2$ (HMVF)/NiCr–MgF$_2$ (LMVF)/MgF$_2$ solar absorber.

| Sublayers | Sputtering method | Ar (sccm) | Sputtering pressure (Pa) | Power (W) | Deposition rate (nm/min) |
|---|---|---|---|---|---|
| NiCr | DC | 100 | 0.1 | 31 | 7.6 |
| MgF$_2$ | RF | 100 | 0.1 | 200 | 5.2 |
| Au | RF | 110 | 2 | 300 | 14 |

**Fig. 2.** (a) Refractive index and (b) absorption coefficient of the NiCr–MgF$_2$ cermet layers with different metal volume fractions calculated by effective medium theory. (c) Refractive index and (d) absorption coefficient of the deposited NiCr–MgF$_2$ cermet layers with metal volume fraction of 0.13 and 0.25 calculated by effective medium theory and measured by reflectance, transmittance and thickness, respectively.

thermal emittance is almost independent on the incident angle.

### 4.2. Experimental deposited solar absorber

#### 4.2.1. Near normal solar absorptance and thermal emittance

Fig. 5 shows the measured reflectance spectrum of the deposited NiCr–MgF$_2$ solar absorber with optimized metal volume fractions and thicknesses, which matches the simulated counterpart very well. The near normal solar absorptance are high up to 0.976 and the near normal thermal emittance at 25 °C are as low as 0.045, which is the best result as far as we know and very close to the limit of simulation. The high normal solar absorptance comes from three near-zero interference minimums which are located in 400–500 nm, 700–800 nm, and 1700–2000 nm, originating from interferences between MgF$_2$, LMVF and HMVF NiCr–MgF$_2$, and Au layers. The first interference minimum located at 400–500 nm results from $\lambda/4$ antireflection of MgF$_2$ as $n_{\mathrm{MgF2}}(\lambda = 400$–$500$ nm)$\approx 1.38$ and $4n_{\mathrm{MgF2}}d_{\mathrm{MgF2}} \approx 4 \times 1.38 \times 84$ nm $\approx 464$ nm. Meanwhile, the third interference minimum located at 1700–2000 nm is due to $\lambda/4$ antireflection of LMVF and HMVF NiCr–MgF$_2$, because $n_{\mathrm{LMVF}}$ and $n_{\mathrm{HMVF}}$ at such wavelength range are about 2.00 and 2.46 and $4(n_{\mathrm{LMVF}}d_{\mathrm{LMVF}} + n_{\mathrm{HMVF}}d_{\mathrm{HMVF}}) \approx 4 \times (2.00 \times 77$ nm $+ 2.46 \times 137$ nm$) \approx 1964$ nm. The second interference minimum located at 700–800 nm is originated from $3\lambda/4$ antireflection of MgF$_2$, LMVF and HMVF NiCr–MgF$_2$ as $4(n_{\mathrm{MgF2}}d_{\mathrm{MgF2}}+n_{\mathrm{LMVF}}d_{\mathrm{LMVF}} + n_{\mathrm{HMVF}}d_{\mathrm{HMVF}})/3 \approx (4 \times 1.38 \times 84$ nm $+ 4 \times 1.84 \times 77$ nm $+ 4 \times 2.01 \times$

137 nm)/3 $\approx 711$ nm. The low normal thermal emittance comes from the low absorptance to IR radiation and the sharp step response from high absorptance to low absorptance at transition wavelength range, which is due to the moderate thickness of HMVF NiCr–MgF$_2$ and high interface reflectance to IR radiation. The minor difference between the experimental and simulated normal solar absorptance results from the deviations between measured and simulated reflectance at 400–600 nm and 1000–1200 nm. Such deviations probably come from the difference of optical constants of Ni, Cr and MgF$_2$ between thin films deposited by magnetron sputtering and counterparts in the database. The extremely small difference between the experimental and simulated normal thermal emittance is due to the deviation between measured and simulated reflectance at $\lambda \geq 15$ μm and such deviation is in tolerance of measurement error of IR spectrometer.

#### 4.2.2. Angular solar absorptance and thermal emittance

Fig. 6 shows the measured solar absorptance and thermal emittance values as a function of incident angle, which matches the simulated values very well. The experimental angular solar absorptance maintains very high values of 0.976–0.957 over a wide angular range from 0° up to 50°. When the incident angle increases from 60° to 80°, the experimental angular solar absorptance value decreases rapidly from 0.922 to 0.609. However, such angular dependence is a common shortcoming of interferometric solar absorber, and 50° is a fairly good result thanks to the low refractive index of MgF$_2$. Moreover, the reflectance in $\lambda \geq 2.5$ μm
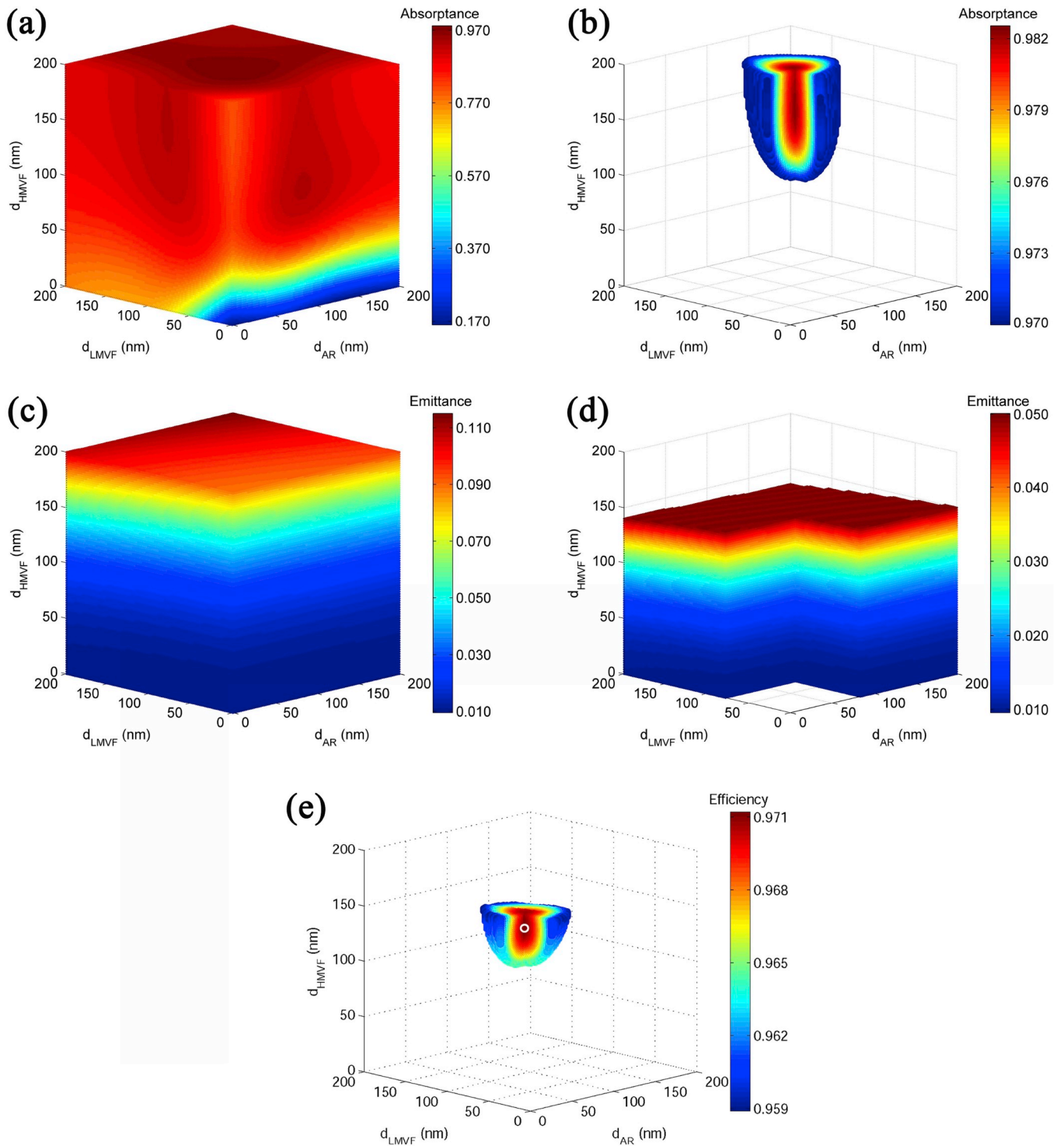
**Fig. 3.** The simulated normal solar absorptance, normal thermal emittance and photo-thermal conversion efficiency as a function of thicknesses of HMVF, LMVF and AR layers. (b) and (d) show the set of dots of [$d_{AR}$, $d_{LMVF}$, $d_{HMVF}$] whose corresponding $\alpha_{sn} \geq 0.970$ and $\varepsilon_n \leq 0.050$, respectively. (e) shows the photo-thermal conversion efficiency $\eta$ in the set of dots of [$d_{AR}$, $d_{LMVF}$, $d_{HMVF}$] whose corresponding $\alpha_{sn} \geq 0.970$ and $\varepsilon_n \leq 0.050$, and the white circle represents the positon of maximal $\eta$.

has slight dependence on incident angle as it is mainly determined by differences of optical constants of all individual, and thus the thermal emittance is almost independent of incident angle. Therefore, the angular thermal emittance has low values of 0.045–0.054 from 0° up to 50°.

## 5. Conclusions

An Au/NiCr–MgF$_2$(HMVF)/NiCr–MgF$_2$(LMVF)/MgF$_2$ spectrally selective solar absorber is designed and fabricated for ultra-high solar absorptance and low thermal emittance. The performance of NiCr–MgF$_2$ solar absorber is simulated using the effective medium theory and film matrix method, and the theoretically optimized NiCr–MgF$_2$ solar

**Table 2**
The theoretically optimized parameters for the Au/NiCr–MgF$_2$ (HMVF)/ NiCr–MgF$_2$ (LMVF)/MgF$_2$ solar absorber.

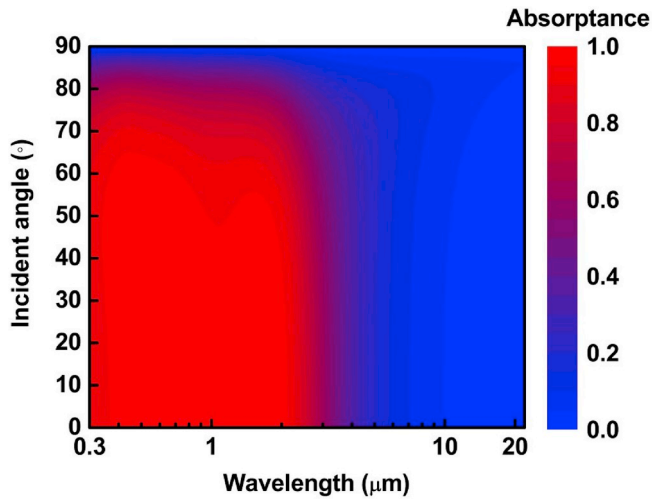| Layer | Material | Metal Volume fraction | Thickness (nm) |
|---|---|---|---|
| AR | MgF$_2$ | 0 | 84 |
| LMVF | NiCr–MgF$_2$ | 0.17 | 77 |
| HMVF | NiCr–MgF$_2$ | 0.32 | 137 |
| IR-reflector | Au | 1 | 100 |



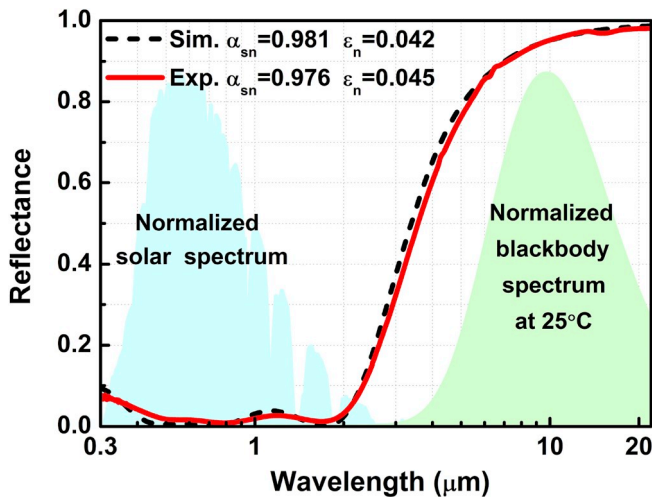**Fig. 4.** Simulated absorptance spectra of the optimized solar absorber at different incident angles from 0° to 90°.



**Fig. 5.** Experimental reflectance spectrum of the deposited solar absorber compared with the simulated one.

absorber has a normal solar absorptance ($\alpha_{sn}$) of 0.981 and a normal thermal emittance ($\varepsilon_n$) of 0.042 at 25 °C. The tandem films of NiCr–MgF$_2$ solar absorber is fabricated by magnetron sputtering and it has an ultra-high near normal solar absorptance of $\alpha_{sn} = 0.976$ and a low near normal thermal emittance of $\varepsilon_n = 0.045$ at 25 °C, which is very close to the simulated limit. Furthermore, the deposited NiCr–MgF$_2$ solar absorber allows a wide incident angle of 50° with $\alpha_s(\theta) \geq 0.957$ and $\varepsilon(\theta) \leq 0.054$. Such spectrally selective solar absorber is an outstanding candidate for solar thermal applications.
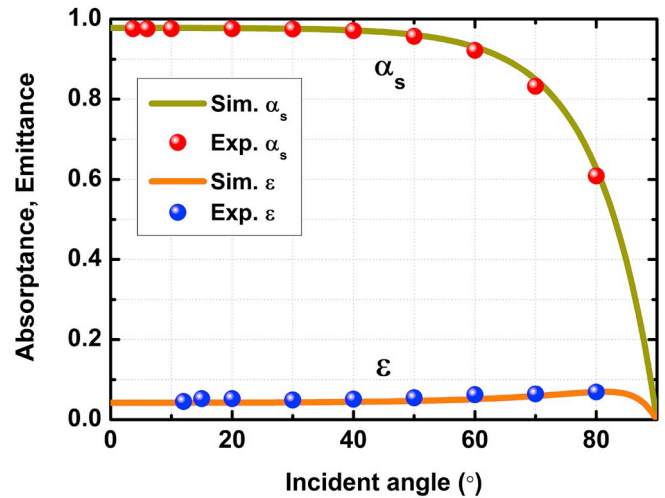


**Fig. 6.** Experimental solar absorptance and thermal emittance values of the deposited solar absorber as a function of incident angle compared with the simulated ones.

## Declaration of competing interest

The authors declare that they have no known competing financial interests or personal relationships that could have appeared to influence the work reported in this paper.

## Appendix A. aSupplementary data

Supplementary data to this article can be found online at https://doi.org/10.1016/j.solmat.2019.110219.

## References

[1] F. Cao, K. McEnaney, G. Chen, Z. Ren, A review of cermet-based spectrally selective solar absorbers, Energy Environ. Sci. 7 (2014) 1615–1627, https://doi.org/10.1039/c3ee43825b.
[2] M. Farchado, J.M. Rodríguez, G. San Vicente, N. Germán, A. Morales, Optical parameters of a novel competitive selective absorber for low temperature solar thermal applications, Sol. Energy Mater. Sol. Cells 178 (2018) 234–239, https://doi.org/10.1016/j.solmat.2018.01.031.
[3] X.H. Gao, X.L. Qiu, X.T. Li, W. Theiss, B.H. Chen, H.X. Guo, T.H. Zhou, G. Liu, Structure, thermal stability and optical simulation of ZrB$_2$ based spectrally selective solar absorber coatings, Sol. Energy Mater. Sol. Cells 193 (2019) 178–183, https://doi.org/10.1016/j.solmat.2018.12.040.
[4] H. Aréna, M. Coulibaly, A. Soum-Glaude, A. Jonchère, A. Mesbah, G. Arrachart, N. Pradeilles, M. Vandenhende, A. Maitre, X. Deschanels, SiC-TiC nanocomposite for bulk solar absorbers applications: effect of density and surface roughness on the optical properties, Sol. Energy Mater. Sol. Cells 191 (2019) 199–208, https://doi.org/10.1016/j.solmat.2018.11.018.
[5] A. Dan, A. Biswas, P. Sarkar, S. Kashyap, K. Chattopadhyay, H.C. Barshilia, B. Basu, Enhancing spectrally selective response of W/WAlN/WAlON/Al$_2$O$_3$-Based nanostructured multilayer absorber coating through graded optical constants, Sol. Energy Mater. Sol. Cells 176 (2018) 157–166, https://doi.org/10.1016/j.solmat.2017.11.013.
[6] I. Heras, E. Guillén, F. Lungwitz, G. Rincón-Llorente, F. Munnik, E. Schumann, I. Azkona, M. Krause, R. Escobar-Galindo, Design of high-temperature solar-selective coatings based on aluminium titanium oxynitrides AlyTi1-y(OxN1-x). Part 1: advanced microstructural characterization and optical simulation, Sol. Energy Mater. Sol. Cells 176 (2018) 81–92, https://doi.org/10.1016/j.solmat.2017.10.015.

[7] F. Cao, D. Kraemer, L. Tang, Y. Li, A.P. Litvinchuk, J. Bao, G. Chen, Z. Ren, A high-performance spectrally-selective solar absorber based on a yttria-stabilized zirconia cermet with high-temperature stability, Energy Environ. Sci. 8 (10) (2015) 3040–3048, https://doi.org/10.1039/C5EE02066B.

[8] K. Zhang, M. Du, L. Hao, J. Meng, J. Wang, J. Mi, X. Liu, Highly corrosion resistant and sandwich-like Si3N4/Cr-CrNx/Si3N4 coatings used for solar selective absorbing applications, ACS Appl. Mater. Interfaces 8 (49) (2016) 34008–34018, https://doi.org/10.1021/acsami.6b11607.

[9] N. Selvakumar, H.C. Barshilia, Review of physical vapor deposited (PVD) spectrally selective coatings for mid-and high-temperature solar thermal applications, Sol. Energy Mater. Sol. Cells 98 (2012) 1–23, https://doi.org/10.1016/j.solmat.2011.10.028.

[10] D. Kraemer, B. Poudel, H.P. Feng, J. Christopher Caylor, B. Yu, X. Yan, Y. Ma, X. Wang, D. Wang, A. Muto, K. McEnaney, M. Chiesa, Z. Ren, G. Chen, High-performance flat-panel solar thermoelectric generators with high thermal concentration, Nat. Mater. 10 (7) (2011) 532, https://doi.org/10.1038/nmat3013.

[11] N. Wang, L. Han, H. He, N.H. Park, K. Koumoto, A novel high-performance photovoltaic–thermoelectric hybrid device, Energy Environ. Sci. 4 (9) (2011) 3676–3679, https://doi.org/10.1039/C1EE01646F.

[12] F. Cao, D. Kraemer, T. Sun, Y. Lan, G. Chen, Z. Ren, Enhanced thermal stability of W-Ni-Al2O3 cermet-based spectrally selective solar absorbers with tungsten infrared reflectors, Adv. Energy Mater. 5 (2) (2015) 1401042, https://doi.org/10.1002/aenm.201401042.

[13] S.R. Atchuta, S. Sakthivel, H.C. Barshilia, Transition metal based CuxNiyCoz-x-yO4 spinel composite solar selective absorber coatings for concentrated solar thermal applications, Sol. Energy Mater. Sol. Cells 189 (2019) 226–232, https://doi.org/10.1016/j.solmat.2018.09.033.

[14] X. Wang, T. Luo, Q. Li, X. Cheng, K. Li, High performance aperiodic metal-dielectric multilayer stacks for solar energy thermal conversion, Sol. Energy Mater. Sol. Cells 191 (2019) 372–380, https://doi.org/10.1016/j.solmat.2018.12.006.

[15] A. AL-Rjoub, L. Rebouta, P. Costa, L.G. Vieira, Multi-layer solar selective absorber coatings based on W/WSiAlNx/WSiAlOyNx/SiAlOx for high temperature applications, Sol. Energy Mater. Sol. Cells 186 (2018) 300–308, https://doi.org/10.1016/j.solmat.2018.07.001.

[16] J. Liu, Z. Sun, H. Wang, Design and characterization of solar absorbing multilayer stack based on Al/Cr-N-O/SiO2 layers, Sol. Energy Mater. Sol. Cells 188 (2018) 18–26, https://doi.org/10.1016/j.solmat.2018.06.013.

[17] Y. Ning, W. Wang, Y. Sun, Y. Wu, Y. Liu, H. Man, M. Malik, C. Wang, S. Zhao, E. Tomasella, A. Bousquet, Effects of substrates, film thickness and temperature on thermal emittance of Mo/substrate deposited by magnetron sputtering, Vacuum 128 (2016) 73–79, https://doi.org/10.1016/j.vacuum.2016.03.008.

[18] Y. Ning, W. Wang, Y. Sun, Y. Wu, Y. Liu, H. Man, C. Wang, Y. Zhang, S. Zhao, E. Tomasella, A. Bousquet, Investigation on low thermal emittance of Al films deposited by magnetron sputtering, Infrared Phys. Technol. 75 (2016) 133–138, https://doi.org/10.1016/j.infrared.2016.01.007.

[19] E. Randich, D.D. Allred, Chemically vapor-deposited ZrB2 as a selective solar absorber, Thin Solid Films 83 (4) (1981) 393–398, https://doi.org/10.1016/0040-6090(81)90646-5.

[20] B.O. Seraphin, Chemical vapor deposition of thin semiconductor films for solar energy conversion, Thin Solid Films 39 (1976) 87–94, https://doi.org/10.1016/0040-6090(76)90626-X.

[21] C.E. Kennedy, Review of mid- to high-temperature solar selective absorber materials, Natl. Renew. Energy Lab., USA, 2002.

[22] J. Wang, Z. Chen, D. Li, Simulation of two-dimensional Mo photonic crystal surface for high-temperature solar-selective absorber, Phys. Status Solidi A 207 (8) (2010) 1988–1992, https://doi.org/10.1002/pssa.200925573.

[23] Q.C. Zhang, High efficiency Al-N cermet solar coatings with double cermet layer film structures, J. Phys. D Appl. Phys. 32 (1999) 1938–1944, https://doi.org/10.1088/0022-3727/32/15/324.

[24] S. Zhao, E. Wäckelgård, Optimization of solar absorbing three-layer coatings, Sol. Energy Mater. Sol. Cells 90 (3) (2006) 243–261, https://doi.org/10.1016/j.solmat.2005.03.009.

[25] Y. Ning, W. Wang, L. Wang, Y. Sun, P. Song, H. Man, Y. Zhang, B. Dai, J. Zhang, C. Wang, Y. Zhang, S. Zhao, E. Tomasella, A. Bousquet, J. Cellier, Optical simulation and preparation of novel Mo/ZrSiN/ZrSiON/SiO2 solar selective absorbing coating, Sol. Energy Mater. Sol. Cells 167 (2017) 178–183, https://doi.org/10.1016/j.solmat.2017.04.017.

[26] C.F. Guo, T. Sun, F. Cao, Q. Liu, Z. Ren, Metallic nanostructures for light trapping in energy-harvesting devices, Light: Sci. Appl. 3 (4) (2014) e161, https://doi.org/10.1038/lsa.2014.42.

[27] S.X. Zhao, Spectrally Selective Solar Absorbing Coatings Prepared by Dc Magnetron Sputtering, PhD. Thesis, Uppsala University, Sweden, 2007, pp. 1651–6214.

[28] C. Nunes, V. Teixeira, M.L. Prates, N.P. Barradas, A.D. Sequeira, Graded selective coatings based on chromium and titanium oxynitride, Thin Solid Films 442 (2003) 173–178, https://doi.org/10.1016/S0040-6090(03)00967-2.

[29] A. Antonaia, A. Castaldo, M.L. Addonizio, S. Esposito, Stability of W-Al2O3 cermet based solar coating for receiver tube operating at high temperature, Sol. Energy Mater. Sol. Cells 94 (2010) 1604–1611, https://doi.org/10.1016/j.solmat.2010.04.080.

[30] Q.C. Zhang, Y.G. Shen, High performance W–AlN cermet solar coatings designed by modelling calculations and deposited by DC magnetron sputtering, Sol. Energy Mater. Sol. Cells 81 (2004) 25–37, https://doi.org/10.1016/j.solmat.2003.08.021.

[31] Y. Ning, W. Wang, Y. Sun, Y. Wu, H. Man, C. Wang, S. Zhao, E. Tomasella, A. Bousquet, Y. Zhang, Tuning of reflectance transition position of Al-AlN cermet solar selective absorbing coating by simulating, Infrared Phys. Technol. 80 (2017) 65–70, https://doi.org/10.1016/j.infrared.2016.11.012.

[32] L. Zheng, F. Zhou, Z. Zhou, X. Song, G. Dong, M. Wang, X. Diao, Angular solar absorptance and thermal stability of Mo-SiO2 double cermet solar selective absorber coating, Sol. Energy 115 (2015) 341–346, https://doi.org/10.1016/j.solener.2015.02.013.

[33] J. Wang, B. Wei, Q. Wei, D. Li, Optical property and thermal stability of Mo/Mo–SiO2/SiO2 solar-selective coating prepared by magnetron sputtering, Phys. Status Solidi A 208 (3) (2011) 664–667, https://doi.org/10.1002/pssa.201026301.

[34] Q.C. Zhang, M.S. Hadavi, K.D. Lee, Y.G. Shen, Zr–ZrO2 cermet solar coatings designed by modelling calculations and deposited by dc magnetron sputtering, J. Phys. D Appl. Phys. 36 (6) (2003) 723, https://doi.org/10.1088/0022-3727/36/6/315.

[35] Q.C. Zhang, D.R. Mills, New cermet film structures with much improved selectivity for solar thermal applications, Appl. Phys. Lett. 60 (5) (1992) 545–547, https://doi.org/10.1063/1.106602.

[36] J. Pastrňák, L. Roskovcová, Refraction index measurements on AlN single crystals, Phys. Status Solidi 14 (1966), https://doi.org/10.1002/pssb.19660140127. K5-K8.

[37] John C.C. Fan, Steven A. Spura, Selective black absorbers using rf-sputtered Cr2O3/Cr cermet films, Appl. Phys. Lett. 30 (1977) 511–513, https://doi.org/10.1063/1.89234.

[38] D.L. Wood, K. Nassau, Refractive index of cubic zirconia stabilized with yttria, Appl. Opt. 21 (1982) 2978–2981, https://doi.org/10.1364/AO.21.002978.

[39] R. Boidin, T. Halenkovič, V. Nazabal, L. Beneš, P. Němec, Pulsed laser deposited alumina thin films, Ceram. Int. 42 (2016) 1177–1182, https://doi.org/10.1016/j.ceramint.2015.09.048.

[40] L. Gao, F. Lemarchand, M. Lequime, Refractive index determination of SiO2 layer in the UV/Vis/NIRJ. Eur. Optical Soc. Rapid Publ. range: spectrophotometric reverse engineering on single and bi-layer designs, J. Eur. Opt. Soc. Rap. Publ. 8 (2013) 13010, https://doi.org/10.2971/jeos.2013.13010.

[41] H.H. Li, Refractive index of alkaline earth halides and its wavelength and temperature derivatives, J. Phys. Chem. Ref. Data 9 (1980) 161–289, https://doi.org/10.1063/1.555616.

[42] X.H. Gao, W. Theiss, Y.Q. Shen, P.J. Ma, G. Liu, Optical simulation, corrosion behavior and long term thermal stability of TiC-based spectrally selective solar absorbers, Sol. Energy Mater. Sol. Cells 167 (2017) 150–156, https://doi.org/10.1016/j.solmat.2017.04.015.

[43] A. Sakurai, H. Tanikawa, M. Yamada, Computational design for a wide-angle cermet-based solar selective absorber for high temperature applications, J. Quant. Spectrosc. Radiat. Transfer 132 (2014) 80–89, https://doi.org/10.1016/j.jqsrt.2013.03.004.

[44] X.H. Gao, Z.M. Guo, Q.F. Geng, P.J. Ma, A.Q. Wang, G. Liu, Enhanced optical properties of TiN-based spectrally selective solar absorbers deposited at a high substrate temperature, Sol. Energy Mater. Sol. Cells 163 (2017) 91–97, https://doi.org/10.1016/j.solmat.2017.01.023.

[45] M.A. Ordal, R.J. Bell, R.W. Alexander, L.L. Long, M.R. Querry, Optical properties of Au, Ni, and Pb at submillimeter wavelengths, Appl. Optic. 26 (1987) 744–752, https://doi.org/10.1364/AO.26.000744.

[46] A.D. Rakić, A.B. Djurišic, J.M. Elazar, M.L. Majewski, Optical properties of metallic films for vertical-cavity optoelectronic devices, Appl. Optic. 37 (1998) 5271–5283, https://doi.org/10.1364/AO.37.005271.

[47] N. Selvakumar, S.B. Krupanidhi, H.C. Barshilia, Carbon nanotube-based tandem absorber with tunable spectral selectivity: transition from near-perfect blackbody absorber to solar selective absorber, Adv. Mater. 26 (2014) 2552–2557, https://doi.org/10.1002/adma.201305070.

[48] Q.C. Zhang, J.C. Kelly, D.R. Mills, Optical studies of germanium implanted with high dose oxygen, J. Appl. Phys. 68 (1990) 4788–4794, https://doi.org/10.1063/1.346135.

[49] H.C. Barshilia, N. Selvakumar, K.S. Rajam, D.V. Sridhara Rao, K. Muraleedharan, A. Biswas, TiAlN/TiAlON/Si3N4 tandem absorber for high temperature solar selective applications, Appl. Phys. Lett. 89 (2006) 191909, https://doi.org/10.1063/1.2387897.

[50] A. Dan, H.C. Barshilia, K. Chattopadhyay, B. Basu, Solar energy absorption mediated by surface plasma polaritons in spectrally selective dielectric-metal-dielectric coatings: a critical review, Renew. Sustain. Energy Rev. 79 (2017) 1050–1077, https://doi.org/10.1016/j.rser.2017.05.062.

[51] N. Selvakumar, K. Rajaguru, G.M. Gouda, H.C. Barshilia, AlMoN based spectrally selective coating with improved thermal stability for high temperature solar thermal applications, Sol. Energy 119 (2015) 114–121, https://doi.org/10.1016/j.solener.2015.06.047.

[52] A. Dan, K. Chattopadhyay, H.C. Barshilia, B. Basu, Angular solar absorptance and thermal stability of W/WAlN/WAlON/Al2O3-based solar selective absorber coating, Appl. Therm. Eng. 109 (2016) 997–1002, https://doi.org/10.1016/j.applthermaleng.2016.04.069.

[53] N. Selvakumar, A. Biswas, K. Rajaguru, G.M. Gouda, H.C. Barshilia, Nanometer thick tunable AlHfN coating for solar thermal applications: transition from absorber to antireflection coating, Sol. Energy Mater. Sol. Cells 137 (2015) 219–226, https://doi.org/10.1016/j.solmat.2015.02.008.

[54] N. Selvakumar, A. Biswas, D.V. Sridhara Rao, S.B. Krupanidhi, H.C. Barshilia, Role of component layers in designing carbon nanotubes-based tandem absorber on metal substrates for solar thermal applications, Sol. Energy Mater. Sol. Cells 155 (2016) 397–404, https://doi.org/10.1016/j.solmat.2016.06.051.